Biomech Model Mechanobiol (2014) 13:615–626
DOI 10.1007/s10237-013-0522-z

ORIGINAL PAPER

Effect of cyclic loading on the nanoscale deformation of hydroxyapatite and collagen fibrils in bovine bone

Anjali Singhal · Stuart R. Stock · Jonathan D. Almer · David C. Dunand

Received: 11 October 2012 / Accepted: 7 August 2013 / Published online: 20 August 2013

Abstract Cyclic compressive loading tests were carried out on bovine femoral bones at body temperature (37 °C), with varying mean stresses (−55 to −80 MPa) and loading frequencies (0.5–5 Hz). At various times, the cyclic loading was interrupted to carry out high-energy X-ray scattering measurements of the internal strains developing in the hydroxyapatite (HAP) platelets and the collagen fibrils. The residual strains upon unloading were always tensile in the HAP and compressive in the fibrils, and each increases in magnitude with loading cycles, which can be explained from damage at the HAP–collagen interface and accumulation of plastic deformation within the collagen phase. The samples tested at a higher mean stress and stress amplitude, and at lower loading frequencies exhibit greater plastic deformation and damage accumulation, which is attributed to greater contribution of creep. Synchrotron microcomputed tomography of some of the specimens showed that cracks are produced during cyclic loading and that they mostly occur concentric with Haversian canals.

Keywords Bone · Fatigue · Synchrotron · X-ray diffraction · Interfacial damage

Electronic supplementary material The online version of this article (doi:10.1007/s10237-013-0522-z) contains supplementary material, which is available to authorized users.

A. Singhal (✉) · D. C. Dunand
Department of Materials Science and Engineering, Northwestern University, Evanston, IL 60208, USA
e-mail: AnjaliSinghal2007@u.northwestern.edu; Anjali.singhal@gmail.com

D. C. Dunand
e-mail: dunand@northwestern.edu

S. R. Stock
Department of Molecular Pharmacology and Biological Chemistry, Feinberg School of Medicine, Northwestern University, Chicago, IL 60611, USA
e-mail: s-stock@northwestern.edu

J. D. Almer
Advanced Photon Source, Argonne National Laboratory, Building 431, 9700 S. Cass Avenue, Argonne, IL 60439, USA
e-mail: almer@aps.anl.gov

1 Introduction

Hard mineralized tissues such as bones are the primary load bearing structures of the body. Bone consists of an organic matrix [about 90 % type I collagen with the rest being made up of non-collagenous proteins and lipids (Fratzl et al. 2004; Olszta et al. 2007)], a mineral phase (carbonated hydroxyapatite, HAP) and water (Simonian et al. 1994), which form a complex structure hierarchically organized from the nano- to the macroscale (Weiner and Wagner 1998), and is capable of supporting physiological loads and resisting fracture. Periodic stresses and strains varying in both intensity and mode (tension or compression) are experienced in physiological activities like walking and running (Lanyon and Smith 1970; Lanyon et al. 1975; Cowin 1989; Burr et al. 1996). Peak compressive stresses (estimated from strain measurements) of −97, −30 and −15 MPa have been recorded in in vivo studies of racing horses (Nunamaker et al. 1990a,b), walking dogs (Rubin and Lanyon 1982) and jogging humans (Mikic and Carter 1995; Burr et al. 1996), respectively. Despite the high strength and toughness, bones can fracture due to impact loads and repetitive or sustained loads exerted over long periods of time (Nunamaker et al. 1990a,b). Fatigue fractures or stress fractures are a special concern for highly active adults (e.g., soldiers and athletes), elderly people and patients with diseased bones (Kulin et al. 2011; Willett et al. 2011). It is thus important to gain a deeper understanding of the mech-

anisms controlling the stresses and strains in the complex hierarchy of structures in bone during cyclical loading, to ultimately predict, prevent or delay such failures.

Cyclic loading results in property degradation in bone caused by the accumulation and propagation of microcracks over a large number of cycles (Yeni and Fyhrie 2002; Moore et al. 2004; Sobelman et al. 2004). The formation of microcracks is dependent on the loading mode (Carter and Hayes 1977; George and Vashishth 2005), where tensile loading results in diffuse microcracks and compressive loading produces more linear microcracks. The fatigue life of cortical bone is greater during compressive cyclic loading than during tensile cyclic loading (Pattin et al. 1996). The stiffness of bone has been shown to decrease during cyclic loading due to the degradation of the HAP–collagen interface, leading to reduced load transfer (Yeni and Fyhrie 2002; Winwood et al. 2006). Furthermore, crack propagation (and hence damage) is also influenced by microstructural features like osteons, cement lines and lamellae (Kim et al. 2007).

The macroscopic behavior of bone during fatigue has been extensively studied, mostly at the macro- or microscopic level, but the interaction between HAP and collagen (in particular the load transfer between these phases) that occurs at the nanoscale remains mostly unexplored. High-energy synchrotron X-ray scattering provides crystal lattice information from the bulk of the sample, unlike nanoindentation or imaging techniques such as scanning and transmission electron microscopy and atomic force microscopy which provide surface structural information by sampling small, near-surface volumes. The use of high-energy X-rays allows in situ testing (Haeffner et al. 2005) and provides strains in the constituting phases of metal-matrix composites (Young et al. 2007) shedding light on load sharing and also recently in biological composites like antlers (Akhtar et al. 2008), bone (Singhal et al. 2011) and dentin (Deymier-Black et al. 2012). Here, this technique is used for the first time to quantify the strains in the constituent phases of bone during cyclic loading in compression and at body temperature.

X-ray microcomputed tomography (micro-CT) has been used to image the microdamage present in fatigued bone samples (Christen et al. 2012). Unlike scanning and transmission electron microscopy, micro-CT images microdamage in three dimensions and provides relationship between cracks and surrounding features (Haversian canals and osteocyte lacunae). Micro-CT has been previously used to study damage and cracking in non-biological samples (e.g., Stock et al. 1992; Guvenilir et al. 1999) and microarchitecture in mouse bones (Martin-Badosa et al. 2003; Peyrin 2009), image crack propagation behavior in human bones (Koester et al. 2008) and assess bone ingrowth in bio-scaffolds (Peyrin et al. 2007). Previously, Voide et al. (2009) and Christen et al. (2012) observed a notched mouse femur under monotonic compressive loading with synchrotron micro-CT at specific strain

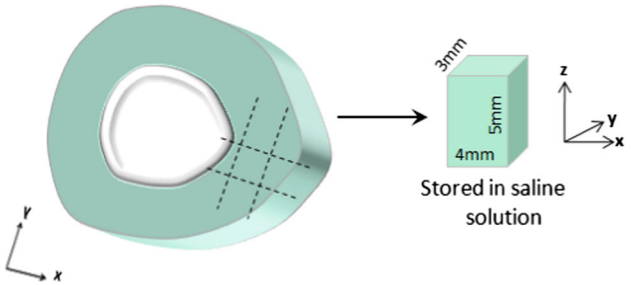

Fig. 1 Schematic showing a transverse cross-section of the femur. The dashed lines show an example of the way the sample is obtained from this cross-section

intervals. Near the notch, linear cracks were seen along the loading direction parallel to the Haversian canals. They also suggested that linear cracks in one plane appeared as diffuse features in another plane. Further, the lacunae served as stress concentration as well as crack blunting sites. The notched sample constrained the cracks to develop near the notch. Here, we use micro-CT to image the samples post-mechanical testing to determine the relationships between the cracks, developed due to cyclic loading only, and the surrounding microstructural features.

2 Materials and methods

2.1 Sample preparation

Fresh bovine femurs were obtained ∼5 h after the 18-month-old, Black Angus cow was slaughtered (Aurora Packing Company Inc., North Aurora, IL). The marrow and attached ligaments were removed using scalpels. The epiphyses of the femur were removed, and rough parallel cuts were made perpendicular to the femur long axis using an autopsy saw to create sections approximately 8 ± 0.5 cm in height. A schematic of this preparation process is illustrated in Fig. 1. These sections were frozen in gauze soaked in phosphate-buffered saline (PBS), at $-20\,^{\circ}$C for ∼1 week. After thawing, parallel cuts were made on one section of the distal right femur about 5.5 mm apart along the femur long axis, using a Buehler Isomet-1000 precision diamond wafering saw operating at low speeds. Each transverse section was then cut into rectangular blocks with dimensions of $5(\pm 0.014) \times 4(\pm 0.009) \times 3(\pm 0.012)$ mm^3. These cutting operations were performed under constant irrigation with deionized (DI) water to prevent the bone from drying. All the samples used in this experiment were taken from the anterio-medial and posterio-medial sides of the femur, as indicated in Table 1. The samples were weighed with a precision balance, after blotting excess PBS with tissue, and their dimensions were measured with a point micrometer, taking an average of three measurements for each dimension. The apparent densities of the samples were calculated as the ratio of mass

Table 1 List of all the samples with their experimental condition during fatigue

Sample	Location	Mean stress (MPa)	Stress amplitude (MPa)	Frequency (Hz)	Number of cycles
A	Anterior	−55	25	0.5	1,810
B	Anterio-medial	−55	25	2	4,630
C	Anterio-medial	−55	25	5	4,630
D	Anterio-medial	−85	25	0.5	280
E	Posterio-medial	−85	25	2	4,630
F	Posterio-medial	−85	25	5	4,630
G	Posterio-medial	−60	35	2	4,630
H	Posterio-medial	−60	45	2	4,630

to volume, calculated from size measurements. The samples were then stored in PBS and frozen at −20 °C until the X-ray experiments were performed (for ∼3 weeks).

2.2 X-ray scattering experiments

These experiments were performed at the Advanced Photon Source (APS), Argonne National Laboratory (Argonne, IL), at beamline 1-ID C. Cyclic uniaxial compression loading tests, with a triangular waveform, were performed in load control on an MTS 858 load frame, with the samples maintained in a hydrated condition at body temperature (37 °C). Six samples were tested with constant stress amplitude of 25 MPa and mean stresses of −55 (samples A–C) or −85 MPa (samples D–F). Cycling was done at frequencies of 0.5, 2 or 5 Hz. Samples G and H were cycled at a mean stress of −60 MPa, loading rate of 2 Hz and stress amplitude of 35 and 45 MPa, respectively. The total number of load cycles accumulated on each sample is listed in Table 1. Due to limited beam time, the samples were subjected to fewer cycles (and without achieving failure) than in most macroscopic fatigue studies mentioned previously (Carter and Hayes 1976; Zioupos et al. 1996; Boyce et al. 1998; George and Vashishth 2005). The plateau in the resulting strain versus time curves suggests that these cycles correspond to the crack propagation stage of fatigue deformation.

The setup of the sample stage and the detectors at the beamline is similar to that reported previously (Singhal et al. 2011). A 65 keV X-ray beam, with a 30 × 35 μm^2 cross-section, was used for the experiment. A GE-41 RT detector, placed at a distance of 698 mm from the sample, with a 2,048 × 2,048 pixel grid (200 × 200 μm^2/pixel), was used to record the wide-angle scattering (WAXS) patterns. A PI CCD detector, placed at a distance of 4,000 mm from the sample, with a 2,048 × 2,048 pixel grid (80 × 80 μm^2/pixel), recorded the small-angle scattering (SAXS) rings. The X-ray exposure times were 15 s for WAXS and 5 s for SAXS. The WAXS detector had to be translated laterally out of the beam to expose the SAXS detector, resulting in a delay of about 30 s between the two measurements. X-ray exposure during each of the 20 s per WAXS+SAXS measurement corresponds to a dose of 132 kGy (Singhal et al. 2011).

The WAXS patterns are produced by diffraction from the crystalline HAP particles from which the average HAP lattice strain can be calculated (Deymier-Black et al. 2010). The SAXS patterns, on the other hand, arise from the density differences produced by the periodic arrangement of HAP platelets in the collagen matrix (∼67 nm collagen D-period) (Almer and Stock 2007). The SAXS-derived strain is referred to as fibrillar strain, since it is representative of a nanoscale composite response. Examples of WAXS and SAXS patterns for similar bovine bone are given in earlier works (Singhal et al. 2011).

Cyclic loading was interrupted intermittently, and the sample was monotonically loaded in eight steps between the minimum and the maximum cyclic stresses to take WAXS and SAXS measurements, the same position being sampled every time. This procedure was repeated 7 times during the cyclic loading. Therefore, each sample thus received a total dose of 7,392 kGy(= 132 × 8 × 7) for the duration of the experiment. With increasing use of synchrotron radiation to investigate the properties of biological materials like bone (Almer and Stock 2007; Neil Dong et al. 2010; Barth et al. 2011), it is becoming important to determine the effect of high irradiation doses. In this study, the effect of high-dose, high-energy synchrotron X-ray irradiation on the fatigue properties of bone will be investigated. The results presented in this paper will thus be analyzed addressing the changes associated not only with damage due to cyclic loading, but also with that due to irradiation.

2.3 Diffraction analysis

The procedure to calculate strain from the diffraction rings has been described in detail elsewhere (Almer and Stock

2005) and is summarized here. WAXS patterns are analyzed using previously developed MATLAB^{TM} programs, where the orientation-dependent deviatoric strains (ε_η) are calculated using the formula:

$$\varepsilon_\eta = \left(r^* - r_\eta\right)/r_\eta \quad (1)$$

where r_η is the radius of the ring at an azimuth η and r^* is the radius of the ring at which strain is invariant as a function of load. The azimuths of 90° and 270° of the diffraction rings are used to calculate the longitudinal strain in the HAP crystals aligned along the femur long axis. The initial residual strain in the fibrils is, by definition, zero. Thus, the fibrillar strain is calculated, using the third-order D-period ring in the SAXS pattern, relative to the radius of the ring when the sample is under zero stress (at the beginning of the experiment). Longitudinal strain is calculated using the scattering ring radius at 90° and 270° azimuths.

The HAP and fibrillar strains, $\varepsilon_{\mathrm{HAP}}$ and $\varepsilon_{\mathrm{Fib}}$, are plotted as a function of applied compressive stress $\sigma_{\mathrm{applied}}$ for different number of cycles. The apparent modulus of the two phases, i.e., the ratio of the applied stress to the lattice strain in HAP ($E_{\mathrm{app}}^{\mathrm{HAP}} = \sigma_{\mathrm{applied}}/\varepsilon_{\mathrm{HAP}}$) or collagen fibril ($E_{\mathrm{app}}^{\mathrm{Fib}} = \sigma_{\mathrm{applied}}/\varepsilon_{\mathrm{Fib}}$), is calculated from a linear least-squares fit of the loading stress–strain data following Refs. (Deymier-Black et al. 2010). The first value of HAP residual strain for each sample was measured at the beginning of the experiment, at zero applied stress. Since the samples were unloaded only to their minimum, nonzero cyclic stress to take WAXS/SAXS measurements, the residual strains at all other cycle numbers are calculated by extrapolating the linear fits on the stress–strain line graphs to zero stress.

2.4 Microcomputed tomography

Synchrotron micro-CT was performed on samples C, F and H at station 2-BM of the APS (Wang et al. 2001). Samples of dimensions $1.5 \times 2 \times 5\,\mathrm{mm}^3$ were extracted from the mechanically tested samples for imaging, using a slow-speed diamond saw (referred to in Sect. 2.1) by longitudinally slicing the sample into half its thickness. The samples were immersed in ethanol and dried prior to imaging, to prevent motion artifacts (Almer and Stock 2005). Data were acquired with 23.8 keV photons, projections were recorded every 0.12° over 180°, and reconstruction was on a $2,048 \times 2,048$ grid with isotropic 0.75 µm voxels using Gridrec (Wang et al. 2001). The micro-CT data are displayed in grayscale with the lighter pixels indicating higher attenuation. The reconstructed 2D slices were visualized using ImageJ or Amira® 3D. The presence of reconstruction artifacts necessitated manual segmentation of the Haversian canals, lacunae and nutrient channels, and cracklike features. The "magic wand" tool in Amira® was used for this manual segmentation process. Stacks of images were used to visualize the cracks in 3D. The volume of the space occupied by the cracks was calculated using Amira, by counting the total number of voxels within the grayscale threshold for the cracks. In a number of instances, the damage features could not be clearly distinguished from the surrounding matrix because of low contrast, making segmentation difficult. Hence, only the most prominent damage features are shown in the results.

2.5 Thermogravimetric analysis

Thermogravimetric analysis (TGA) was performed to determine the weight and volume fraction of HAP, collagen and water in the samples, as reported previously (Singhal et al. 2011). After mechanical testing, a 3–10 mg piece of each sample was cut from approximately the same volume as the diffraction measurements. The samples were heated from 25 to 680 °C at a rate of 10 °C/min and held at 680° for 10 min prior to cooling. The weight fractions were obtained by determining the start and end points of the phase decomposition, i.e., where the derivative of the curve becomes zero (25, 225 and 550 °C). The experimental weight fractions were then converted to volume fractions using density values of 3.2, 1.1 and 1.0 g/cm^3 for HAP, collagen and water, respectively (Martin et al. 1998). To determine the uncertainty in measurement, TGA was performed twice on samples D and G, taking small volumes adjacent to each other. The average difference of the mineral, collagen and water values obtained from the repeat measurements above is taken as the uncertainty. The volume fractions of the three phases in each sample along with the uncertainty estimates are shown in Table 2.

3 Results

Figure 2 shows applied stress as a function of strain in HAP and collagen fibrils for sample B, after accumulating 0, 30, 160, etc. (up to 4,630) loading cycles. Upon initial loading of the sample from 0 to −42 MPa, strains of −0.16 and −0.19 % are measured in HAP and fibrils, respectively. The initial apparent moduli $E_{\mathrm{app}}^{\mathrm{HAP}}$ and $E_{\mathrm{app}}^{\mathrm{Fib}}$ are calculated to be 29.8 ± 1.9 and 18.5 ± 1.6 GPa, respectively. With subsequent cycling between −30 and −80 MPa, HAP and fibrillar strains, as measured at each stress, drift in opposite directions, i.e., the compressive strain in the HAP phase decreases toward zero and ultimately becomes slightly tensile, while that in the fibrils increases (i.e., it becomes more compressive). All the samples (A–H) tested under different cyclic loading conditions exhibit a similar stress–strain trend. However, the rates at which the strains change depend upon the loading condition on the sample, as described in the following sections.

Table 2 List of the samples with their densities and volume fractions, and parameter c_1 for HAP (Eq. 2) which is used to fit the residual strains

Sample	Density (g/cm^3)	Volume fraction (%)			$c_1 (\times 10^{-6})$
		HAP	Collagen	Water	
A	2.06	42	37	21	69 ± 50
B	2.03	41	37	22	157 ± 56
C	2.02	39	39	23	94 ± 28
D	2.05	39	36	25	–
E	2.02	40	38	23	294 ± 190
F	2.10	43	36	21	139 ± 77
G	2.02	40	38	22	216 ± 12
H	2.07	42	37	22	175 ± 22
Std.	0.02	0.4	0.6	0.5	–

The uncertainties in the values of c_1 are the standard errors from regression fits
"Std." refers to the standard deviation of the density and volume fraction values for all the samples

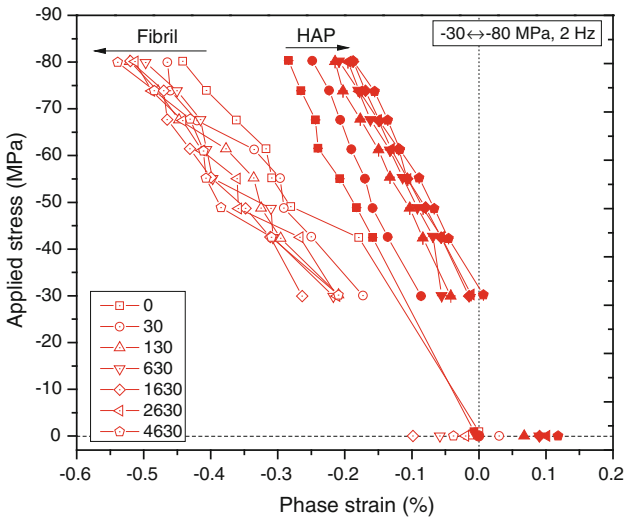

Fig. 2 Plots of applied stress versus phase strain for HAP and the fibril on loading of sample B. The legend shows the number of cycles corresponding to the *symbols*. The *arrows* indicate the direction of translation of the *curves*. The data points (not connected by *lines*) shown at zero stress are the residual strains extrapolated from the *stress–strain curves* of the corresponding *symbols*

3.1 Effect of frequency and mean stress

3.1.1 HAP residual strains

The evolution of the residual strain in the HAP phase is studied to determine the extent of relaxation in the HAP (and thus collagen) phase. Figure 3a, b shows the residual strains in HAP as a function of the load cycle number at the three frequencies (0.5, 2 and 5 Hz) for the two stress ranges (samples A–C and D–F). Sample D failed after 280 cycles and thus has fewer data points than the other five samples. For all six samples, the HAP residual strains are initially close to zero, become rapidly more tensile up to about 130 cycles and thereafter increase more slowly. This trend is best estimated by a semi-logarithmic equation for the residual strain ε_{res} versus number of loading cycles N, as shown in the inset in Fig. 3a for sample B:

$$\varepsilon_{res} = c_1 \ln(N) + k_1 \quad (2)$$

where k_1 is a constant and c_1 is the slope of the fitted curve. This type of equation was used in Carter and Hayes (1976); Kruzic and Ritchie (2008) to correlate stress amplitude versus number of cycles to failure in macroscopic fatigue tests. The slopes are listed for all samples (except D which failed early) in Table 2.

Figure 3c is a plot of the residual strain (with respect to an initial value defined as zero, as described in Sect. 2.3) in the fibrils for samples A–C. The fibril residual strains have much larger errors due to the lower signal-to-noise ratio, making it difficult to obtain best-fit slope values for residual strain versus cycles. In all samples (A–H), however, the fibril strains increase (i.e., become more compressive) with load cycles.

A single sample was tested with cycles between −30 and −80 MPa, at a frequency of 2 Hz, as shown in Supplementary Figure S1. This sample was loaded to −80 MPa and unloaded to zero stress for measurement of apparent moduli and residual strains. The residual strains in this sample are not extrapolated. The residual strains in this sample decrease toward zero from an initial state of compression. This trend confirms the methodology of using extrapolated residual strains in lieu of measured residual strains in this paper.

3.1.2 Irradiation

Figure 3d shows residual strains of HAP in samples A, B and C versus radiation dose. The strains increase (become more tensile) rapidly up to a dose of 5,500 kGy and at a slower rate at higher doses. The fibril strains, despite their larger errors, show an increase in compressive strains with dose.

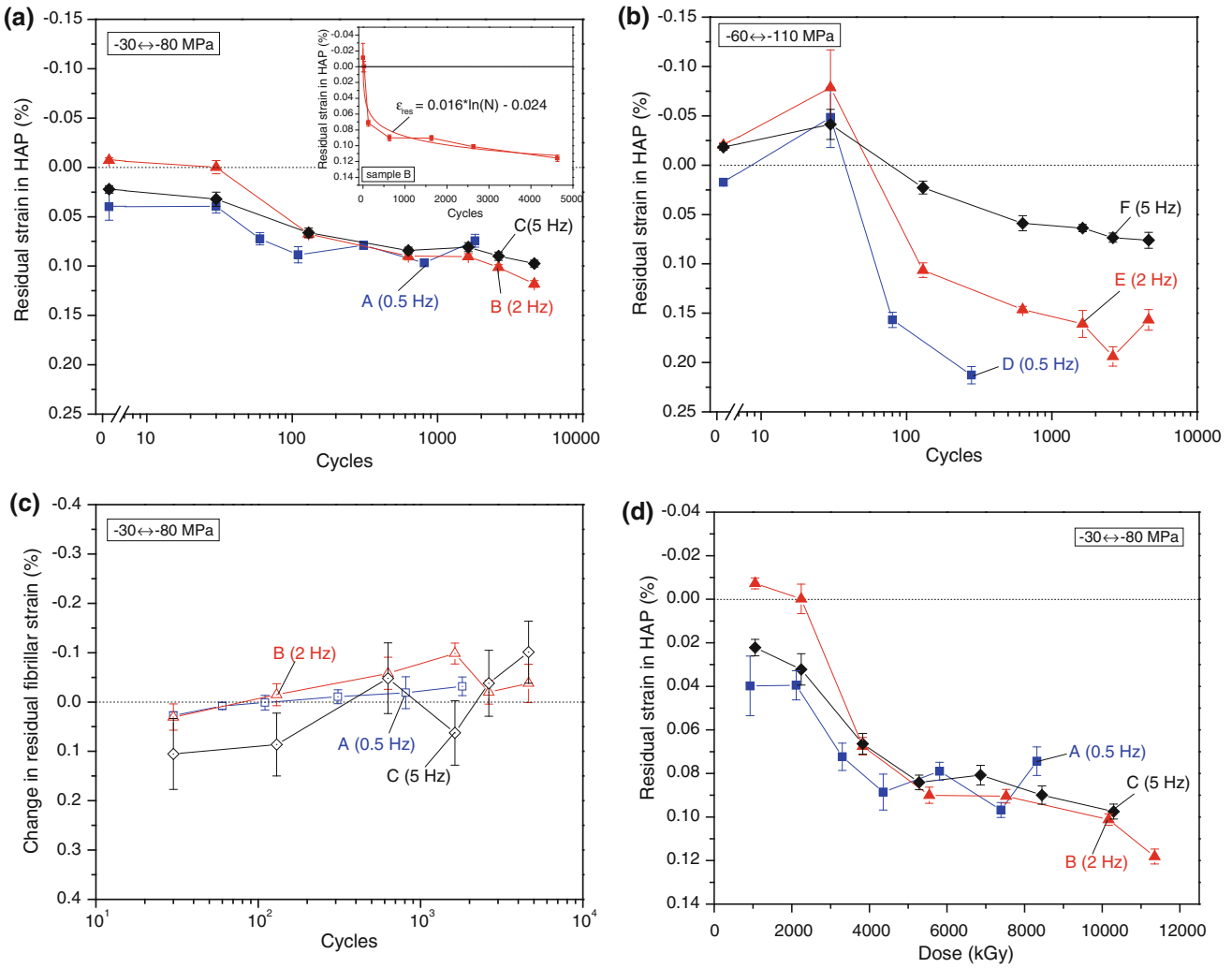

Fig. 3 Plots of HAP residual strain versus number of loading cycles for **a** samples A–C (−30 ↔ −80 MPa), **b** D–F (−60 ↔ −110 MPa). The *error bars* in (**a**) and (**b**) are the errors propagated from standard deviations of nonlinear least-squares fitting of the diffraction peak centers. **c** Plot of change in fibrillar residual strains versus number of loading cycles for samples A–C. **d** Plot of HAP residual strains versus dose for samples A–C. An example fit to calculate c_1 is shown in the *inset* of **a**. The error bars in (**c**) and (**d**) are the errors propagated from the apparent modulus calculation during extrapolation of the *stress–strain line* to zero stress. The *error bar* on the first data point in each *line* series is propagated from standard deviation of nonlinear *least-squares* fitting of the diffraction peak center

3.2 Effect of stress amplitude on residual strain

Figure 4 is a plot of the residual strains in HAP and fibrils as a function of loading cycles for samples G and H, which were tested at constant 2 Hz frequency and −60 MPa mean stress for two stress amplitudes, 35 and 45 MPa. As shown in Fig. 4, the HAP residual strain shows a rapid increase (in tension) up to 500 cycles, after which the rate of increase slowed. The increases in residual strains for samples G and H are also more pronounced compared with samples A–F, as can be seen from the larger values of c_1 from Table 2. Also shown in Fig. 4 is the fibrillar residual strains in these samples which become more compressive with increase in the number of cycles, similar to that seen for samples A–F.

3.3 Microcomputed tomography

Figure 5 shows representative microstructural images of samples C and F which underwent cyclic loading. Figure 5a–c is reconstructed image slices showing a plane perpendicular to the loading direction; Fig. 5d–f is 3D renderings of the volume around the 2D slices shown in Fig. 5a–c, respectively, and provides a better visualization of the features. Figure 5a, d shows a crack between two Haversian canals on the top left and bottom right indicated by the blue arrows. The crack is not visible for the entire distance. Figure 5b, e shows a crack concentric with the Haversian canal of an osteon (indicated by the arrow) which is near a resorption cavity on the top right corner in the image. The spatial and contrast resolution does

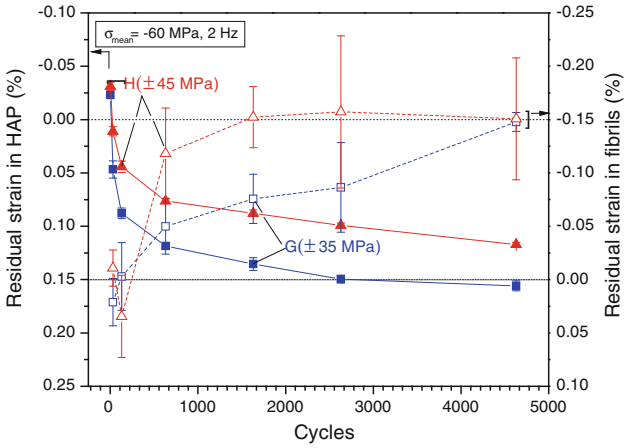

Fig. 4 HAP residual strain (*solid lines*) and change in fibrillar residual strains (*dashed lines*) versus number of loading cycles. The *error bars* are the errors propagated from the apparent modulus calculation during extrapolation of the *stress–strain line* to zero stress. The *error bar* on the first data point in each *line* series is propagated from standard deviation of nonlinear *least-squares* fitting of the diffraction peak center

not allow one to see the exact crack path, i.e., whether the crack propagates along a lamellar interface or within a single lamella. Figure 5c, f shows cracks in between two osteons which are indicated by blue arrows.

Figure 5g shows a histogram containing the number of occurrences of cracks near each microstructural site within each sample. The volume of each visible crack, as calculated by Amira, ranges between 800 and 32,000 μm^3 for the three samples tested, with the majority of the cracks following osteonal geometry concentric with Haversian canals, or occurring at Haversian canals and lacunae, as seen from the histogram. The average crack opening width (in the plane of the 2D slice and perpendicular to the long axis of the sample) is $3.13 \pm 0.67\,\mu m$ ($n = 49$). Crack paths presumably following osteonal geometry are extensively observed in sample C which was tested at lower stresses than samples F and H. Most of the cracks in samples F and H, on the other hand, appear to pass through the microstructural features like lacunae and canals.

4 Discussion

The different apparent moduli of the HAP phase and collagen fibrils in Fig. 2 indicate load partitioning between HAP and collagen: The HAP phase, because it is stiffer than collagen, has lower strains (and thus a higher apparent modulus) than the more compliant HAP/collagen composite fibril (Singhal et al. 2011). Upon continued cycling, the HAP strains at a given applied stress become less compressive, while the fibrillar strains become more compressive (Fig. 1). Increasing macroscopic strains and hysteresis energy [defined as the area between the loading and unloading curves of each cycle (Leng et al. 2009)] during cycling were reported in previous studies of cortical bone, where the bone samples failed between 250 and 10,000 cycles depending on the mode of loading, stress amplitude and frequency of loading (Carter and Hayes 1977; Carter and Caler 1985; Zioupos et al. 1996; Winwood et al. 2006).

The evolution of the fibril residual strains (Fig. 1) indicates the accumulation of plastic deformation in the fibril; the fibrils are nanoscale composites of HAP and collagen which are thus similar to discontinuously reinforced metal-matrix composites where macroscopic strain accumulates with fatigue cycles (Wang and Chim 1983; Bao and McMeeking 1994). In the case of bone under compressive stress cycling, the collagen molecules not only contract elastically, but also undergo viscoelastic and/or plastic compressive deformation through molecular sliding which is not fully recovered on unloading (Folkhard et al. 1987; Sasaki et al. 1998). This results in accumulation of plastic residual strains in the composite collagen fibril, with increase in cycles. A concomitant increase in compressive residual strains in the reinforcement phase would be expected for a composite where the matrix undergoes compressive plastic deformation and thus transfers increasing compressive stresses to the stiffer reinforcement through a well-bonded interface. This increases the load carrying ability of the composite, as shown for example in Al/SiC composites in Withers et al. (1989) and Allen et al. (1992). The load-induced compressive plastic deformation of the matrix thus puts the reinforcement in residual compression and the matrix in residual tension upon unloading (Allen et al. 1992). Plastic deformation and cyclic softening have been commonly observed during fatigue testing of metals and have been described by the Coffin–Manson relationship (Cooper and Fine 1984). By contrast, in this work, the opposite effect is observed: The HAP elastic residual strains become more tensile with cyclic loading. This effect, which can be explained if interfacial damage and relaxation processes take place within the matrix and the interface, is discussed in the following sections.

Irradiation has deleterious effects on the strength, post-yield and fracture toughness properties of cortical bone (Currey et al. 1997; Barth et al. 2010, 2011), through the production of free radicals from hydrolysis of water in the collagen framework, thus increasing the collagen cross-linking. The work by Akkus and Belaney (2005) is, to the authors' knowledge, the only one which studies the effect of irradiation on the fatigue behavior of bone. They show that gamma irradiation (an average dose of 36 kGy) reduces the fatigue life of human cortical bone in tension by two orders of magnitude, which is hypothesized to occur due to the irradiation-induced degradation of the properties of the collagen phase.

Earlier work by the authors and their collaborators investigated the effect of radiation dose on the apparent elastic

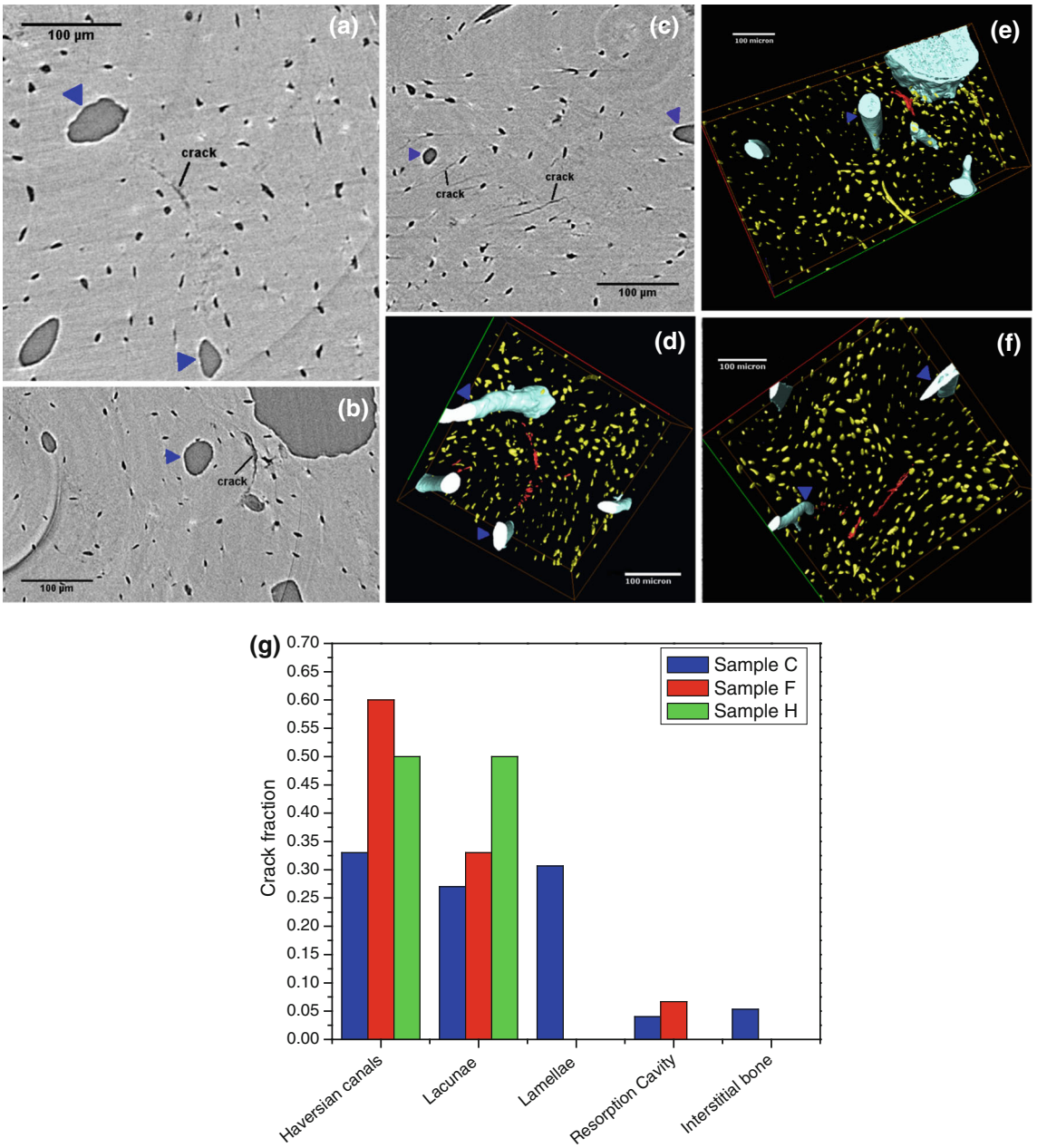

Fig. 5 **a**–**c** 2D reconstructed images and **d**–**f** their corresponding 3D renditions showing: **a**,**d** a crack [labeled in (**a**) and colored *red* in (**d**)] near two Haversian canals (shown by *blue arrows*) in sample F; **b**, **e** a crack [labeled in (**b**) and colored *red* in (**e**)] at the lamellar interface of an osteon in sample C; **c**, **f** cracks [labeled in (**c**) and colored *red* in (**f**)] near two Haversian canals (shown by *blue arrows*) in the interstitial bone in sample C. **g** Histogram showing the incidence of cracks near each of the microstructural features in sample C, F and H

modulus and residual strains of bovine cortical bone (Singhal et al. 2011), where samples were monotonically loaded and unloaded for a maximum of 10 cycles at a uniform rate. It was found that the magnitude of the compressive residual strains in the HAP phase decrease significantly as a function of dose up to 3,800 kGy. This change was hypothesized to occur due to the degradation of the HAP/collagen interface (which is composed of various types of interactions such as ionic, hydrogen, Van der waals and water surface tension), caused by the decarboxylation of collagen side chains bound to the HAP platelets via calcium-mediated ionic bonds, as first suggested by Hubner et al. (2005). This irradiation-induced interfacial debonding thus weakens the interface and allows the collagen molecules to slide, resulting in a reduction in the compressive strains carried by the HAP phase.

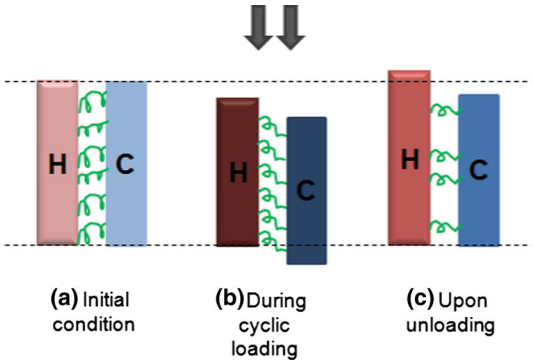

Fig. 6 Schematic illustrating residual strains in the HAP (H) and collagen phases (labeled H and C, respectively). **a** Both phases have an initial residual strain state of zero as indicated by most of the data in this study. **b** On application of cyclic load, the HAP and collagen phase are compressed and the collagen phase slides resulting in stretching of interfacial bonds. **c** Upon unloading, relaxation in the collagen and at the HAP/collagen interface puts the HAP phase in residual tension and collagen in residual compression. Also, the load- and irradiation-induced debonding on unloading is indicated by the reduced number of bonds at the interface. The *dashed lines* serve as a guide to compare the relative strain states between the three conditions **a**–**c**

The deformation mechanism proposed in the present work is illustrated through a schematic in Fig. 6. The average initial HAP residual strains in the samples A–H is about $-25\,\mu\varepsilon$; this is treated as being nearly zero in Fig. 6a since an average value of $-1{,}426\,\mu\varepsilon$ has been found in our previous study (Singhal et al. (2011)). The initial residual strain in the fibrils is defined as zero, as described in Sect. 2.3. Upon cyclic loading, both phases initially deform elastically. Irradiation-induced damage weakens the HAP/collagen interface, thus allowing the collagen molecules to slide (Fig. 6b). This weak interface is further weakened by the shear stresses generated during cyclic loading, which results in breakage of Van der Waals and hydrogen bonds at the interface. During unloading, HAP undergoes elastic strain recovery, while the viscoelastic collagen undergoes a time-dependent compressive strain recovery process. At the ultra-structural level, this involves recovery of the molecular contraction, as well as recovery of the molecular rearrangement that might have taken place due to the slippage of the collagen molecules with each other. The recovery from molecular contraction takes place on a shorter time scale than that from rearrangement processes (Folkhard et al. 1987; Sasaki et al. 1998). Thus, as the molecules expand upon unloading (or relax from compression), they pull on the HAP–collagen interface applying tensile stresses to the HAP platelets. This puts the HAP in residual tension once the completely unloaded stage is reached, as shown in Fig. 6c. As this inelastic deformation in the collagen fibril (nanocomposite) and interfacial damage due to mechanical loading and irradiation increases with cycles, the tensile residual strains in HAP also increase.

The diffraction strains presented in this work are not separable between the intra-fibrillar and extra-fibrillar HAP populations. The percentage distribution of HAP crystals between these two fibrillar spaces has been found to vary significantly with some works suggesting that as high as 77 % of HAP is found in the extra-fibrillar region (Bonar et al. 1985; Sasaki et al. 2002). A recent work by Poundarik et al. (2012) has shown the formation of dilatational bands between the osteocalcin and osteopontin molecules binding mineral aggregates found outside the fibrils, which result in ellipsoidal voids during the deformation process. This process is suggested to occur before any inter-fibrillar deformation. It is speculated that the change in residual strains measured by diffraction could be the relaxation of these extra-fibrillar mineral aggregates.

The diffraction data collection procedure in the present work supplies an average dose of about 7,000 kGy per sample during measurement. However, the change in the volume sampled by the X-rays, with a beam cross-section of $30 \times 35\,\mu m^2$, due to permanent macroscopic compression of the sample during cyclic loading, will result in the above reported dose to be spread out as opposed to being concentrated on a single volume. One way to circumvent this issue of accumulation of dose at a single location in the sample is to take an array of measurements spread out over multiple locations in the sample, as done in our recent work on creep in bone (Deymier-Black et al. 2011). Change in load transfer behavior, indicative of damage accumulation at the HAP–collagen interface, has been shown to occur at ∼115 kGy (Deymier-Black et al. 2011). Therefore, in the present study, the high number of load cycles, the high mean stress and the very high radiation doses are expected to cause damage within collagen as well as the HAP–collagen interface. Because each sample accumulates the same irradiation dose, comparison of the effect of changing loading variables is thus valid. However, conclusions about the physiological behavior of bone cannot be made.

4.1 Effect of frequency, mean stress and stress amplitude on residual strains

For both mean stresses examined, the samples tested at 2 Hz (samples B and E) showed a higher rate of increase in HAP residual strains with respect to the cycles than those tested at 5 Hz (samples C, F), as seen from the greater values of c_1 in Table 2. The higher mean and maximum stresses experienced by samples E and F result in greater interfacial damage and plastic deformation in collagen as compared to samples B and C (Fig. 3a, b). Sample C also exhibited smaller values of c_1 compared with sample G and H which were tested at the lower frequency of 2 Hz, again indicating greater increase in HAP residual strains at lower frequencies. Higher frequency loading for the same stress range results in a shorter dwell time at each stress for a given number of cycles (Zioupos et

al. 2001). Deformation of collagen is strain rate-dependent (Peterlik et al. 2006), and higher strain rate allows less time for collagen sliding and thus less plastic deformation and damage accumulation. Also, for the same number of loading cycles, samples B and E, which were tested at lower frequencies (hence over longer times), show a greater rate of increase in residual strains than the higher frequencies samples C and F, respectively (tested over shorter times). This suggests that a time-dependent deformation mechanism is dominant at these loading cycles. Results from additional samples tested at these conditions would be needed to further support this case.

The HAP residual strain in samples G and H (from the posterior-medial region), tested at −60 MPa mean stress and 2 Hz frequency (Fig. 4b), exhibits a greater change with respect to cycle number compared to samples A–F. For the same loading frequency, the greater stress amplitude (and thus stress range) of samples G and H (35 and 45 MPa, respectively, Fig. 4) compared to samples B and E (25 MPa) results in more significant changes in the residual strains. The HAP residual strain in samples G and H becomes tensile [from—(0.02–0.03) % initially to 0.12–0.16 % after 4,630 cycles], and this can be explained by the interfacial damage and plastic deformation of the collagen molecules (as described in Sect. 4.1). Samples G and H differ solely by their stress amplitudes (35 and 45 MPa, respectively, Fig. 4); the deformation mechanism in this case (Fig. 4) is affected by a combination of two variables—dwell time and cycling stresses. The greater c_1 value (Table 2) of sample G suggests greater interfacial damage compared to sample H, indicating the dominance of the first factor in the relaxation mechanism. However, the lower HAP volume fraction of sample G as compared to sample H (by 2 %) confounds the above hypothesis since G, being more compliant, would plastically deform to a larger extent (Currey 1984, 1988). Hence, additional samples would be needed to conclusively discern a trend in this case.

4.2 Damage morphology

Micro-CT assessed the microstructural damage in some of the cyclic load tested samples and correlated the damage with the loading conditions. The cracks shown in Fig. 5 are similar to those typically seen during compressive loading, i.e., they are linear and occur along the loading direction (Reilly and Currey 1999; Winwood et al. 2006). These cracks have been speculated as arising from shear forces acting along microstructural interfaces like the lamellae which are arranged in a radial pattern around the Haversian canal (Zioupos and Currey 1994; O'Brien et al. 2003). The tensile strains in the transverse direction due to the Poisson's effect open these cracks and lower the load transfer across these interfaces, thus compromising the integrity of the structure. Osteon pullout has been observed in cases of severe debonding between the osteonic lamellae (Vashishth et al. 2000). Although a measure of the change in the macroscopic modulus of the samples with cycles is not available in our study, the presence of microcracks suggests stiffness degradation in the samples (Pattin et al. 1996; Boyce et al. 1998; Burr et al. 1998; Sobelman et al. 2004). The average crack opening observed in this study is ∼3 μm. Typically, cracks in synchrotron micro-CT data sets can be detected with openings as low as one quarter of the voxel dimension (Stock 2008). Here, the voxel size is ∼0.75 μm, and the resolving power is ∼1 μm. A high density of nanocracks, i.e., cracks at the ultra-structural level, as delaminations of the HAP–collagen interface, cannot be excluded by the micro-CT data. This kind of interfacial separation has been hypothesized to exist by Fleck and Eifler (2003) and has been invoked in the previous sections to explain the change in the residual strains observed in our samples. Such damage at the ultra-structural level has been detected as a characteristic whitening in trabecular bone as observed through high-speed photography techniques and found to be associated with debonding of collagen fibrils (Thurner et al. 2007; Sun et al. 2010).

Comparison of damage morphology between samples C, F and H (Fig. 5a–c, g) shows that the former has extensive cracking along paths concentric with the Haversian canal of an osteon, whereas the latter two exhibit cracks that penetrate the osteons and lacunae. This can be rationalized to some extent by the different stresses to which the samples were subjected. The maximum cyclic stress on sample C was by 31–38 % lower than that in samples F and H (see Table 1) and would thus have a lower crack propagation rate (Behiri and Bonfield 1980). At lower crack propagation rates, the crack is more susceptible to arrest at microstructural boundaries like the lamellar interfaces. Higher loading rates result in higher local stresses and a crack propagating at a higher rate, as is the case for samples F and H. Such a crack would be driven by the normal stress component and bypass these microstructural features (Fleck and Eifler 2003). However, care must be taken while making this comparison because the volumes of the samples imaged represent only 6 % of the entire sample volume. Thus, the damage morphology observed in these volumes might not be prevalent throughout the sample.

One of the main limitations of the present work is the limited number of samples investigated for each experimental condition. However, the consistent trends in the HAP and fibrillar strains lead us to suggest mechanisms for deformation at the nanoscale level in bone due to cyclic loading. Additional samples would need to be investigated in order to establish trends which are more statistically significant for the different parameters examined. Nano-CT imaging with voxel sizes substantially below 1 μm is needed. This statistical nature of the nanocracking is a further challenge: Nano-CT necessarily images much smaller volumes than micro-CT, exacerbating

the sampling issues mentioned above. Thus, the applicability of this technique remains limited by its resolution and the size of the sample which can be imaged.

5 Conclusions

This high-energy X-ray diffraction study examines in bovine cortical bones the effect of accumulating compressive loading cycles at body temperature (37 °C) upon the strains, both residual and in response to compressive loading, within the HAP platelets and at the fibrillar level.

- The original near-zero HAP residual strains become more tensile as loading cycles accumulate. This is interpreted to be due to accumulating damage at the HAP–collagen interface and plastic deformation within the collagen matrix, pointing toward both mechanical and radiation damage. A concomitant increase in the magnitude of the compressive residual fibrillar strains is due to accumulation of viscoelastic and/or permanent deformation as cyclic loading proceeds.
- Damage accumulation during cyclic loading, as observed by a change in residual strain in the HAP platelets, depends on the frequency of loading, stress amplitude and the mean stress. The samples tested at greater stress amplitudes, higher mean stresses and lower frequencies showed the greatest damage where the HAP residual strains increased in tension with cycles due to damage accumulation resulting from rapid loading (possibly delamination at the HAP/collagen interface).
- Micro-CT results complement the strain results obtained from *in situ* cyclic loading tests. Microcracks were observed at microstructural inhomogeneities and interfaces.

Acknowledgments The authors thank Prof. L. Catherine Brinson (NU), Dr. Alix Deymier-Black (NU) and Mr. Fang Yuan (NU) for numerous useful discussions throughout this work. They further acknowledge Mr. Yuan and Dr. Deymier-Black for their assistance with the diffraction experiments at the APS-1ID. They also acknowledge Dr. Xianghui Xiao (APS) for his help with the micro-CT experiments at APS-2BM. Use of the Advanced Photon Source was supported by the US Department of Energy, Office of Science, Office of Basic Energy Sciences, under Contract No. DE-AC02-06CH11357.

References

Akhtar R, Daymond MR et al (2008) Elastic strains in antler trabecular bone determined by synchrotron X-ray diffraction. Acta Biomater 4(6):1677–1687

Akkus O, Belaney RM (2005) Sterilization by gamma radiation impairs the tensile fatigue life of cortical bone by two orders of magnitude. J Orthop Res 23(5):1054–1058

Allen AJ, Bourke MAM et al (1992) The analysis of internal strains measured by neutron diffraction in Al/SiC metal matrix composites. Acta Metallurgica et Materialia 40(9):2361–2373

Almer JD, Stock SR (2005) Internal Strains and stresses measured in cortical bone via high-energy X-ray diffraction. J Struct Biol 152(1):14–27

Almer JD, Stock SR (2007) Micromechanical responses of mineral and collagen phases in bone. J Struct Biol 157(2):365–370

Bao G, McMeeking RM (1994) Fatigue crack growth in fiber-reinforced metal-matrix composites. Acta Metall Mater 42(7):2415–2425

Barth HD, Launey ME et al (2010) On the effect of x-ray irradiation on the deformation and fracture behavior of human cortical bone. Bone 46(6):1475–1485

Barth HD, Zimmermann EA et al (2011) Characterization of the effects of x-ray irradiation on the hierarchical structure and mechanical properties of human cortical bone. Biomaterials 32(34):8892–8904

Behiri JC, Bonfield W (1980) Crack velocity dependence of longitudinal fracture in bone. J Mater Sci 15(7):1841–1849

Bonar LC, Lees S et al (1985) Neutron diffraction studies of collagen in fully mineralized bone. J Mol Biol 181:265–270

Boyce TM, Fyhrie DP et al (1998) Damage type and strain mode associations in human compact bone bending fatigue. J Bone Joint Surg 16(3):322–329

Burr DB, Milgrom C et al (1996) In vivo measurement of human tibial strains during vigorous activity. Bone 18(5):405–410

Burr DB, Turner CH et al (1998) Does microdamage accumulation affect the mechanical properties of bone? J Biomech 31(4):337–345

Carter DR, Hayes WC (1976) Fatigue life of compact bone—I. Effects of stress amplitude, temperature and density. J Biomech 9(1):27–34

Carter DR, Hayes WC (1977) Compact bone fatigue damage. Clin Orthop Relat Res 127:265–274

Carter DR, Caler DE (1985) A cumulative damage model for bone fracture. J Orthop Res 3(1):84–90

Christen D, Levchuk A et al (2012) Deformable image registration and 3D strain mapping for the quantitative assessment of cortical bone microdamage. J Mech Behav Biomed Mater 8:184–193

Cooper CV, Fine ME (1984) Coffin-Manson relation for fatigue crack initiation. Scripta Metallurgica 18(6):593–596

Cowin SC (1989) Bone mechanics. CTC Press, Boca Raton

Currey JD (1984) Effects of differences in mineralization on the mechanical properties of bone. Philos Trans R Soc Lond B Biol Sci 304(1121): 509–518

Currey JD (1988) The effect of porosity and mineral content on the Young's modulus of elasticity of compact bone. J Biomech 21(2):131–139

Currey JD, Foreman J et al (1997) Effects of ionizing radiation on the mechanical properties of human bone. J Orthop Res 15(1):111–117

Deymier-Black AC, Almer JD et al (2010) Synchrotron X-ray diffraction study of load partitioning during elastic deformation of bovine dentin. Acta Biomater 6(6):2172–2180

Deymier-Black AC, Yuan F et al (2011) Evolution of load transfer between hydroxyapatite and collagen during creep deformation of bone. Acta Biomater 8(1):253–261

Deymier-Black AC, Stock SR et al (2012) Variability in the elastic properties of bovine dentin at multiple length scales. J Mech Behav Biomed Mater 5(1):71–81

Fleck C, Eifler D (2003) Deformation behaviour and damage accumulation of cortical bone specimens from the equine tibia under cyclic loading. J Biomech 36(2):179–189

Folkhard W, Mosler E et al (1987) Quantitative analysis of the molecular sliding mechanism in native tendon collagen- time-resolved dynamic studies using synchrotron radiation. Int J Biol Macromol 9: 169–175

Fratzl P, Gupta HS et al (2004) Structure and mechanical quality of the collagen-mineral nano-composite in bone. J Mater Chem 14(14): 2115–2123

George WT, Vashishth D (2005) Damage mechanisms and failure modes of cortical bone under components of physiological loading. J Orthop Res 23(5):1047–1053
Guvenilir A, Breunig TM et al (1999) New direct observations of crack closure processes in Al-Li 2090 T8E41. Philos Trans R Soc Lond A Math Phys Eng Sci 357(1761):2755–2775
Haeffner DR, Almer JD et al (2005) The use of high energy X-rays from the Advanced Photon Source to study stresses in materials. Mater Sci Eng A 399(1–2):120–127
Hubner W, Blume A et al (2005) The influence of X-ray radiation on the mineral/organic matrix interaction of bone tissue: an FT-IR microscopic investigation. Int J Artif Organs 28(1):66–73
Kim JH, Miinomi M et al (2007) Fatigue properties of bovine compact bones that have different microstructures. Int J Fatigue 29(6):1039–1050
Koester KJ, Ager JW et al (2008) The true toughness of human cortical bone measured with realistically short cracks. Nat Mater 7:672–677
Kruzic JJ, Ritchie RO (2008) Fatigue of mineralized tissues: cortical bone and dentin. J Mech Behav Biomed Mater 1(1):3–17
Kulin RM, Jiang F et al (2011) Effect of age and loading rate on equine cortical bone failure. J Mech Behav Biomed Mater 4(1):57–75
Lanyon LE, Smith RN (1970) Bone strain in the tibia during normal quadrupedal motion. Acta Orthop Scand 41(3):238–248
Lanyon LE, Hampson WGJ et al (1975) Bone deformation recorded in vivo from strain gauges attached to the human tibial shaft. Acta Orthop Scand 46(2):256–268
Leng H, Dong XN et al (2009) Progressive post-yield behavior of human cortical bone in compression for middle-aged and elderly groups. J Biomech 42:491–497
Martin RB, Burr DB et al (1998) Skeletal tissue mechanics. Springer, New York
Martin-Badosa E, Amblard D et al (2003) Excised bone structures in mice: imaging at three-dimensional synchrotron radiation micro CT1. Radiology 229(3):921–928
Mikic B, Carter DR (1995) Bone strain gage data and theoretical models of functional adaptation. J Biomech 28(4):465–469
Moore TLA, O'Brien FJ et al (2004) Creep does not contribute to fatigue in bovine trabecular bone. J Biomech Eng 126(3):321–329
Neil Dong X, Almer JD et al (2010) Post-yield nanomechanics of human cortical bone in compression using synchrotron X-ray scattering techniques. J Biomech 44(4):676–682
Nunamaker DM, Butterweck DM et al (1990a) Fatigue fractures in thoroughbred racehorses: relationships with age, peak bone strain and training. J Orthop Res 8:604–611
Nunamaker DM, Butterweck DM et al (1990b) Fatigue fractures in thoroughbred racehorses: relationships with age, peak bone strain and training. J Orthop Res 8(4):604–611
O'Brien FJ, Taylor D et al (2003) Microcrack accumulation at different intervals during fatigue testing of compact bone. J Biomech 36(7):973–980
Olszta MJ, Cheng X et al (2007) Bone structure and formation: a new perspective. Mater Sci Eng R 58:77–116
Pattin CA, Caler WE et al (1996) Cyclic mechanical property degradation during fatigue loading of cortical bone. J Biomech 29(1):69–79
Peterlik H, Roschger P et al (2006) From brittle to ductile fracture of bone. Nat Mater 5:52–55
Peyrin F, Mastrogiacomo M et al (2007) SEM and 3D synchrotron radiation micro-tomography in the study of bioceramic scaffolds for tissue-engineering applications. Biotechnol Bioeng 97(3):638–648
Peyrin F (2009) Investigation of bone with synchrotron radiation imaging: from micro to nano. Osteoporos Int 29:1057–1063
Poundarik AA, Diab T et al (2012) Dilatational band formation in bone. Proc Nat Acad Sci 109(47):19178–19183
Reilly GC, Currey JD (1999) The development of microcracking and failure in bone depends on the loading mode to which it is adapted. J Exp Biol 202(5):543–552
Rubin CT, Lanyon LE (1982) Limb mechanics as a function of speed and gait: a study of functional strains in the radius and tibia of horse and dog. J Exp Biol 101(1):187–211
Sasaki N, Shukunami N et al (1998) Time-resolved X-ray diffraction from tendon collagen during creep using synchrotron radiation. J Biomech 32:285–292
Sasaki N, Tagami A et al (2002) Atomic force microscopic studies on the structure of bovine femoral cortical bone at the collagen fibril-mineral level. J Mater Sci Mater Med 13(3):333–337
Simonian PT, Conrad EU et al (1994) Effect of sterilization and storage treatments on screw pullout strength in human allograft bone. Clin Orthop Relat Res 302:290–296
Singhal A, Deymier-Black A et al (2011) Effect of high-energy X-ray doses on bone elastic properties and residual strains. J Mech Behav Biomed Mater 4(8):1774–1786
Sobelman OS, Gibeling JC et al (2004) Do microcracks decrease or increase fatigue resistance in cortical bone? J Biomech 37(9):1295–1303
Stock SR, Breunig TM et al (1992) Nondestructive X-ray tomographic microscopy of damage in various continuous-fiber metal matrix composites. American Society for Testing and Materials, Philadelphia
Stock SR (2008) Microcomputed tomography: methodology and applications. CRC, Boca Raton
Sun X, Hoon Jeon J et al (2010) Visualization of a phantom post-yield deformation process in cortical bone. J Biomech 43(10):1989–1996
Thurner PJ, Erickson B et al (2007) High-speed photography of compressed human trabecular bone correlates whitening to microscopic damage. Eng Fract Mech 74(12):1928–1941
Vashishth D, Tanner KE et al (2000) Contribution, development and morphology of microcracking in cortical bone during crack propagation. J Biomech 33(9):1169–1174
Voide R, Schneider P et al (2009) Time-lapsed assessment of microcrack initiation and propagation in murine cortical bone at submicrometer resolution. Bone 45(2):164–173
Wang SS, Chim ES-M (1983) Fatigue damage and degradation in random short-fiber SMC composite. J Compos Mater 17(2):114–134
Wang Y, Carlo FD et al (2001) A high-throughput x-ray microtomography system at the Advanced Photon Source. Rev Sci Instrum 72(4):2062–2068
Weiner S, Wagner HD (1998) The material bone: structure-mechanical function relations. Ann Rev Mater Sci 28(1):28
Willett TL, Wynnyckyj C et al (2011) The fatigue resistance of rabbit tibiae varies with age from youth to middle age. Osteoporos Int 22(4):1157–1165
Winwood K, Zioupos P et al (2006) Strain patterns during tensile, compressive, and shear fatigue of human cortical bone and implications for bone biomechanics. J Biomed Mater Res Part A 79(2):289–297
Withers PJ, Stobbs WM et al (1989) The application of the eshelby method of internal stress determination to short fibre metal matrix composites. Acta Metall 37(11):3061–3084
Yeni YN, Fyhrie DP (2002) Fatigue damage-fracture mechanics interaction in cortical bone. Bone 30(3):509–514
Young ML, Almer JD et al (2007) Load partitioning between ferrite and cementite during elasto-plastic deformation of an ultrahigh-carbon steel. Acta Mater 55(6):1999–2011
Zioupos P, Currey JD (1994) The extent of microcracking and the morphology of microcracks in damaged bone. J Mater Sci 29(4):978–986
Zioupos P, Wong XT et al (1996) Experimental and theoretical quantification of the development of damage in fatigue tests of bone and antler. J Biomech 29(8):989–1002
Zioupos P, Currey JD et al (2001) Tensile fatigue in bone: are cycles-, or time to failure, or both, important? J Theor Biol 210(3):389–399